

PAPER • OPEN ACCESS

## P3HT vs Spiro-OMeTAD as a hole transport layer for halide perovskite indoor photovoltaics and self-powering of motion sensors

To cite this article: Shaoyang Wang *et al* 2023 *J. Phys. Mater.* **6** 024004

View the [article online](#) for updates and enhancements.

You may also like

- [Recent advances of two-dimensional material additives in hybrid perovskite solar cells](#)

Yifan Yin, Yuchen Zhou, Miriam H Rafailovich et al.

- [Interfacial engineering for organic and perovskite solar cells using molecular materials](#)

Anastasia Soulati, Apostolis Verykios, Konstantina-Kalliopi Armadorou et al.

- [Ultrafast Terahertz Probes of Charge Transfer and Recombination Pathway of CH<sub>3</sub>NH<sub>3</sub>PbI<sub>3</sub> Perovskites](#)

Hui-Jie Yan, , Zhi-Liang Ku et al.



## OPEN ACCESS

RECEIVED  
12 November 2022REVISED  
3 April 2023ACCEPTED FOR PUBLICATION  
5 April 2023PUBLISHED  
19 April 2023

Original content from  
this work may be used  
under the terms of the  
[Creative Commons  
Attribution 4.0 licence](#).

Any further distribution  
of this work must  
maintain attribution to  
the author(s) and the title  
of the work, journal  
citation and DOI.



## PAPER

## P3HT vs Spiro-OMeTAD as a hole transport layer for halide perovskite indoor photovoltaics and self-powering of motion sensors

Shaoyang Wang<sup>1</sup>, Byeong-Cheol Kang<sup>2</sup>, Sang-Joon Park<sup>2</sup>, Tae-Jun Ha<sup>2,\*</sup>   
and Lethy Krishnan Jagadamma<sup>1,\*</sup> <sup>1</sup> Energy Harvesting Research Group, School of Physics & Astronomy, SUPA, University of St Andrews, North Haugh, St Andrews, KY16 9SS Fife, United Kingdom<sup>2</sup> Department of Electronic Materials Engineering, Kwangwoon University, Seoul 01897, Republic of Korea

\* Authors to whom any correspondence should be addressed.

E-mail: [taejunha0604@gmail.com](mailto:taejunha0604@gmail.com) and [lkj2@st-andrews.ac.uk](mailto:lkj2@st-andrews.ac.uk)**Keywords:** P3HT, hole transport layer, stability, halide perovskiteSupplementary material for this article is available [online](#)

## Abstract

Recent years have witnessed the emergence of indoor photovoltaic (PV) devices with the rapid development of the Internet of things technology field. Among the candidates for indoor PVs, halide perovskites are attracting enormous attention due to their outstanding optoelectronic properties suitable for indoor light harvesting. Here we investigated the indoor PV properties of CH<sub>3</sub>NH<sub>3</sub>PbI<sub>3</sub>-based devices using Spiro-OMeTAD and P3HT as the hole transport layers. The Spiro-OMeTAD-based devices show a consistently higher power conversion efficiency under indoor illumination and 1 sun, with the champion devices showing a power conversion efficiency of 21.0% and 30.1% for the forward and reverse scan under 1000 lux warm white LED illumination. Fewer trap states and higher carrier lifetime were revealed for Spiro-OMeTAD based devices compared to P3HT. The best-performed Spiro-OMeTAD-based devices are used to self-power a wearable motion sensor, which could detect human motion in real-time, to create a primary sensor system with independent power management. By attaching the Spiro-OMeTAD indoor PV device to the strain sensor, the sensor exhibits an accurate and sensitive response with finger bending movements with good repeatability and negligible degradation of mechanical stability, which indicates the success of sensor powering with the indoor PV device.

## 1. Introduction

The Internet of things (IoT) is attracting huge interest as the key pillar to achieve an intelligent and modernized society. IoT refers to the networked and interconnected devices to sense and control data automatically and wirelessly [1–3]. Smart sensor systems and wireless communications are key concepts to realize the vision of the IoT ecosystem, which includes various types of wireless sensors, Bluetooth beacons and radio-frequency identification tags. Significant progress has been made in various fields including medical, manufacturing, infrastructure and energy industries [4]. With the rapid development of the IoT, billions of microelectronic wireless sensors and devices are expected to be installed to sense and control data [3]. Noticeably, half of these IoT components will be installed inside the buildings to realize smart and energy-secured buildings. The numerous amount of these devices, which are potentially going to reach one trillion nodes, raise a challenge to build a sustainable and reliable powering system to support them to operate [2]. Currently, the battery-based powering system has various drawbacks including limited lifetime, additional maintenance and interrupted operation and potential environmental harm. Hence, indoor photovoltaic (PV) devices which harvest light energy inside the buildings are considered promising to overcome the issue.

Indoor PVs, which convert indoor ambient light energy from artificial light sources into electricity, are attracting particular attention to develop a convincing indoor self-powering system for IoT devices. Continuously decreasing power requirement for the IoT components allows the sensors to operate only with micro- to milli-watt range of power, which an efficient indoor PV device could easily fulfil. To ensure reliable self-powering of the IoT components, indoor PVs have to meet certain requirements: high efficiency, low cost, energy reliability, deployability, durability and environmental sustainability [2]. Recent years have witnessed rapid progress in indoor PV; different types of PV materials including Si, III–V, CIGS, organic, dye-sensitized, and halide perovskite have been considered as promising candidates for indoor PV research and market [5–10]. The crystalline and microcrystalline silicon PVs, exhibit only low power conversion efficiency (PCE) ( $\sim 9\%$ ) due to their non-ideal bandgap and defects [11–13]. However, a PCE of 36% has been recently reported for hydrogenated amorphous silicon (a-Si:H) thin film solar cells under white LED illumination of 3000 lux [5]. III–V materials based solar cells have achieved a higher PCE of 21% under indoor white LED light, with  $\text{Al}_{0.2}\text{Ga}_{0.8}\text{As}$  as the active layer [8]. However, the high fabrication cost of III–V materials hinders their further application for the PV industry, especially for wide-area devices [2, 13]. Superior efficiencies have been achieved by the solution-based PVs: dye-sensitized solar cells (DSSC), organic photovoltaics (OPV) and halide perovskites [14–18]. Recently Lee *et al* have demonstrated a PCE of 30% under 500 lux LED illumination for the OPVs [14]. DSSCs with 25% PCE under 900 lux fluorescence lamp illumination were also recently reported [18]. However, the limited selection of dye and liquid electrolytes are the remaining problems to improve the stability and reduce the fabrication cost for DSSC [19]. The sensitivity to moisture, and oxygen and the high cost of photoactive materials for OPV also challenge their application for indoor PVs [20].

Halide perovskites, as an emerging family of semiconductor material, are receiving significant attention due to their outstanding optoelectronic properties: high absorption coefficient ( $10^5\text{--}10^7\text{ cm}^{-1}$ ) [21], long carrier diffusion length ( $>1000\text{ nm}$ ) and high defect tolerance [22]. Importantly, the bandgap tunability of halide perovskite allows the material to adjust the bandgap to fit the indoor illumination spectra better. The PCEs for single junction indoor perovskite PV devices have reached 20%–40% [9]. Dagar *et al* have achieved a PCE of 26.9% (output power of  $41.6\text{ }\mu\text{W cm}^{-2}$ ) with a conventional  $\text{MAPbI}_3$  perovskite PV device under 400 lux LED light input of  $300\text{ }\mu\text{W cm}^{-2}$  [23]. Recently, Guo *et al* have developed a  $\text{CsPbI}_2\text{Br}$  perovskite PV device and achieved 32% PCE, corresponding to a maximum power output density of  $93\text{ }\mu\text{W cm}^{-2}$  under 1000 lux LED light ( $300\text{ }\mu\text{W cm}^{-2}$ ) [24]. Table S1 summarizes the performance metrics of recent indoor perovskite PV devices, which shows the flexibility of active layer composition and the superior power conversion efficiency under indoor lighting. Considering the outstanding indoor PV performance, and other potential attributes such as low cost, simple fabrication process, and the fitness for scalable and flexible fabrication, halide perovskite has become one of the most promising candidates for the indoor PV industry. However, our recent investigation has shown that under indoor lighting conditions, halide perovskite PVs demonstrate different  $J\text{--}V$  hysteresis compared to 1 sun illumination and the extent of deviation depends on the selection of the photoactive layers and the charge transport layers [25]. For the halide perovskite indoor PVs to be reliably employed as an efficient self-powering source for the IoT sensors, the  $J\text{--}V$  hysteresis needs to be suppressed.

Typically, in a perovskite PV device, the photoactive layer is sandwiched between two types of charge carrier transport layers: the hole transport layer (HTL) and the electron transport layer (ETL). The selection of transport layer material is an important topic for both PV research and industry since it can determine the power conversion efficiency, fabrication cost and performance stability. The most commonly used HTL material in the halide perovskite PVs is 2,2',7,7'-tetrakis(N,N-di-p-methoxyphenylamine)-9,9'-spirobifluorene (spiro-OMeTAD) [26]. Extraordinary performance is achieved by devices employing spiro-OMeTAD as HTL. However, it requires multiple steps of chemical doping to improve the conductivity and hole extraction efficiency [27, 28]. In addition to that, an oxidation process for 10–24 h is also required to reach the optimal work function [29]. The use of dopants and a long oxidation process complicates the fabrication process and makes it less attractive for scalable fabrication. Other promising HTL materials are PTAA [poly[bis(4-phenyl)(2,4,6-trimethyl-phenyl)amine], poly-TPD [poly(4-butylphenyldiphenylamine)] and poly(3-hexylthiophene) (P3HT) [30]. Among these, P3HT is particularly important because of its excellent optoelectronic properties, low cost, scalability and further, P3HT does not require any additional doping for efficient hole extraction [31]. Both PTAA and poly-TPD are less industry friendly due to their high cost and relatively low performance compared to Spiro-OMeTAD [32]. Despite the promising attributes of P3HT as HTL under 1 sun, its performance under indoor lighting conditions is still unclear. Understanding its hole extraction properties under indoor lighting and a comparison with that of Spiro-OMeTAD HTL based devices under indoor illumination is important for scalable indoor PV development. Hence, in this study, we investigated the performance of spiro-OMeTAD and P3HT HTL based

halide perovskite indoor PV devices under 1000 lux illumination of warm white LED lamp and demonstrated the self-powering of a motion sensor using the devices with better efficiency.

## 2. Experimental details

### 2.1. Materials

CH<sub>3</sub>NH<sub>3</sub>I was purchased from Greatcell solar. PbI<sub>2</sub> was purchased from Alfa Aesar. SnO<sub>2</sub> colloidal dispersion (CAS 18282-10-5) for the ETL was purchased from Alfa Aesar. Hole transport materials including [2,2',7,7'-Tetrakis[N,N-di(4-methoxyphenyl)amino]-9,9'-spirobifluorene (Spiro-OMeTAD, >99% purity), 4-tert-butyl pyridine (tBP, 96% purity), lithium-bis(tri-fluoromethanesulfonyl)imide (Li-TFSI, 99.95% purity) and tris(2-(1H-pyrazol-1-yl)-4-tert-butylpyridine)cobalt(III) tri[bis(trifluoromethane)sulfonimide] (FK 209) were purchased from Ossila, Sigma Aldrich and Greatcell Solar Materials, respectively. The single-walled carbon nanotubes (SWCNTs) (length range: 0.1–4  $\mu$ m, diameter range: 1.2–1.7 nm) and trichloro-(1H,1H,2H,2H-perfluorooctyl) silane (97%) were purchased from Sigma-Aldrich. The polydimethylsiloxane (PDMS) kit (SYLGARD™ 184 Silicone Elastomer Kit) were purchased from Dow.

### 2.2. Device fabrication

Pre-patterned indium tin oxide (ITO) coated glass substrates were sequentially cleaned by sodium dodecyl sulphate solution, deionized water, acetone and isopropyl alcohol with sonication. The substrates were then cleaned with oxygen plasma for 3 min with a Plasma Asher. SnO<sub>2</sub> colloidal dispersion was diluted in deionized water with a volume ratio of 1:6.5 to prepare the SnO<sub>2</sub> electron transport material, 100  $\mu$ l SnO<sub>2</sub> prepared solution is then deposited onto the cleaned substrates by spin-coating at 3000 rpm for 30 s, followed by a thermal annealing process at 150 °C for 30 min to form a compact hole-blocking SnO<sub>2</sub> layer. CH<sub>3</sub>NH<sub>3</sub>PbI<sub>3</sub> perovskite precursor solution was prepared by dissolving CH<sub>3</sub>NH<sub>3</sub>I (1 M; 159 mg) and PbI<sub>2</sub> (1 M; 461 mg) in 66  $\mu$ l of DMSO and 636  $\mu$ l of DMF and stirred at room temperature for 1 h. For the preparation of CH<sub>3</sub>NH<sub>3</sub>PbI<sub>3</sub> perovskite active layer, 90  $\mu$ l of perovskite precursor solution was deposited onto the SnO<sub>2</sub>/ITO/glass substrates via spin-coating at 4000 rpm for 30 s, a diethyl ether anti-solvent washing was carried out onto the perovskite layer at the first 7th second during spin-coating. The spin-coated films were treated by thermal annealing at 100 °C under vacuum for 1 min, followed by an ambient N<sub>2</sub> thermal annealing at 100 °C for 2 min in a nitrogen-filled glove box (O<sub>2</sub> content below 1 ppm).

For the preparation of the HTL, Spiro-OMeTAD solution was prepared by dissolving 72.3 mg Spiro-OMeTAD in 1 ml chlorobenzene, mixed with 28.8  $\mu$ l tBP, 17.5  $\mu$ l Li-TFSI (52 mg Li-TFSI in 100  $\mu$ l acetonitrile) and 29  $\mu$ l FK209 (30 mg FK209 in 100  $\mu$ l acetonitrile). Fifty-five microlitres of prepared Spiro-OMeTAD HTL solution was spin-coated onto the perovskite layer at 4000 rpm for 30 s. The fabricated glass/ITO/SnO<sub>2</sub>/perovskite/Spiro-OMeTAD samples were kept in a desiccator at room temperature for oxygen doping of Spiro-OMeTAD for 12 h. For the preparation of the HTL P3HT, 10 mg P3HT was dissolved in 1 ml chlorobenzene and stirred at room temperature for 1 h. The P3HT solution was filtered by a 0.2  $\mu$ m PTFE filter before spin coating. Ninety microlitres of the P3HT HTL solution was spin-coated onto the perovskite layer at 3000 rpm for 30 s. Finally, a 60 nm thick Au electrode was thermally evaporated (chamber pressure  $3 \times 10^{-6}$  mbar) on top of the HTL.

Figure S2 illustrates the fabrication process flow for the SWCNT-based motion sensor. First, a PDMS solution was synthesized by mixing the base and curing agent in a ratio of 10:1. The mixture was degassed in a vacuum chamber for 1 h to remove the air bubbles, the presence of which can adversely affect the stretchability and mechanical robustness [33]. Next, the mixture was spin-coated onto the wafer substrate and cured at 80 °C for 1 h in air, where the wafer substrate was pre-treated with trichloro-(1H,1H,2H,2H-perfluorooctyl) silane to ensure an easy detachment from the PDMS substrate. After detaching from the wafer substrate, 40  $\mu$ m thick SWCNT random networks were screen-printed using a screen mask with a size of 0.5 cm  $\times$  2 cm, followed by annealing at 100 °C for 10 min in air. Finally, 50 nm thick gold electrodes were deposited via e-beam evaporator to form a contact pad connected with wires to both ends of the SWCNT thin film.

### 2.3. Characterization

The current density-voltage (*J*–*V*) characterization of the fabricated devices was carried out by illuminating the PV device under a ‘warm white’ LED bulb with a colour temperature of 2700 K. The intensity of the warm white LED was fixed to 0.32 mW cm<sup>−2</sup>, corresponding to 1000 lux. An Optometer P9710 and ILT 960 spectroradiometer were used to calibrate the irradiance level. One sun *J*–*V* measurements were carried out by using a solar simulator with xenon arc lamp (150 W, 50  $\times$  50 mm, Class AAA, Sciencetech Solar simulator) at the irradiance level of 100 mW cm<sup>−2</sup> (AM 1.5 G). The measurement active area of the devices was defined by a customized aperture mask of 0.05 cm<sup>2</sup>. The current–voltage measurement settings were

selected as follows: voltage settling time: 0.2 s; voltage increment: 0.05 V; scan rate: 0.2 V s<sup>-1</sup>. For the maximum power point tracking (MPPT) measurement, the devices were characterized under the same conditions for *J*-*V* characteristics and were maintained under the maximum power point condition for 3 min to obtain the MPPT PCE. For the shelf-life stability measurement, the unencapsulated devices were kept under dark, at ambient conditions inside a dry air desiccator (with a relative humidity of 11%) at room temperature (22 °C).

The external quantum efficiency (EQE) measurements were carried out at zero bias by using a monochromatic light, which was obtained by attaching the dual-grating monochromator to a xenon arc lamp. A silicon photodiode made by National Physical Laboratory was used to calibrate the incident photons at each wavelength. The number of incident photons was calculated for each wavelength by using a National Physical Laboratory calibrated silicon photodiode. Light intensity-dependent *J*-*V* measurement, transient photovoltage (TPV) and transient photocurrent (TPC) measurement were carried out with the characterization platform, Paios, Fluxim AG, Switzerland.

Cyclic bending tests of the motion sensor were carried out using a custom-made bending/stretching measurement machine connected to a sourcemeter (Keithley Instrument, Keithley 2400). The self-powering motion sensors were patterned into lines with a width of 0.5 cm, a length of 2 cm and a thickness of 40 μm.

### 3. Results and discussion

#### 3.1. PV properties and characterization of Spiro-OMeTAD and P3HT indoor PVs

To compare the indoor PV performance of Spiro-OMeTAD and P3HT devices, PV devices were fabricated in typical n-i-p device architecture (ITO/SnO<sub>2</sub>/CH<sub>3</sub>NH<sub>3</sub>PbI<sub>3</sub>/Spiro-OMeTAD or P3HT/Au) with CH<sub>3</sub>NH<sub>3</sub>PbI<sub>3</sub> as the photoactive layer. The *J*-*V* characterizations were carried out both under a 1000 lux indoor warm white LED (0.32 mW cm<sup>-2</sup>, the corresponding irradiance spectrum is shown in figure S1) and 1 sun illumination condition. The dependence of PV performance parameters on incident light intensity has been previously reviewed [34–37]. Figure 1 shows the results from the *J*-*V* characterization measurements. Under indoor lighting condition, the Spiro-OMeTAD based devices show a champion PCE of 21.0% and 30.1% for forward and reverse scans, respectively. In contrast, P3HT-based devices exhibit significantly lower champion PCE (forward: 16.4%; reverse: 20.4%) from figure 1(a). The corresponding *V*<sub>OC</sub> is increased from 0.77 V and 0.80 V for P3HT device to 0.84 V and 0.87 V for forward and reverse scans, and *J*<sub>SC</sub> is increased from 0.10 mA cm<sup>-2</sup> and 0.08 mA cm<sup>-2</sup> to 0.14 mA cm<sup>-2</sup> and 0.13 mA cm<sup>-2</sup> for Spiro-OMeTAD devices as shown in figure 1(a). Under indoor lighting condition, the average PCE of Spiro-OMeTAD devices reach 17.8% and 27.5% for forward and reverse scan direction while P3HT devices show an average indoor lighting PCE of 12.2% and 15.4%, respectively as shown in figure 1(b). The corresponding PV performance parameters for the two types of devices are shown in figure S3, it can be seen that both *V*<sub>OC</sub> and *J*<sub>SC</sub> are significantly improved when moving from P3HT to Spiro-OMeTAD. Under indoor lighting conditions, the *J*<sub>SC</sub> of Spiro-OMeTAD devices reaches 0.14 mA cm<sup>-2</sup> and 0.13 mA cm<sup>-2</sup> for different scan directions, while P3HT devices show only 0.10 mA cm<sup>-2</sup> and 0.08 mA cm<sup>-2</sup>.

As for the performance under 1 sun condition, figure 1(c) shows the *J*-*V* curves of the best-performed device for the P3HT devices and Spiro-OMeTAD devices. The PCE for Spiro-OMeTAD is 12.8% and 13.4% for forward and reverse bias, which is significantly higher than 7.2% and 9.0% for the P3HT HTL based device. The most improved PV parameter is *J*<sub>SC</sub>, which increased from 15.4 mA cm<sup>-2</sup> and 14.0 mA cm<sup>-2</sup> to 21.8 mA cm<sup>-2</sup> and 21.2 mA cm<sup>-2</sup> for Spiro-OMeTAD devices as shown in figure 1(c). *V*<sub>OC</sub> also shows an improvement from 0.88 V and 0.91 V for forward and reverse scan for P3HT device to 0.94 V and 0.90 V for the Spiro-OMeTAD devices. Figure 1(d) shows the PCE distribution under 1 sun for both types of devices. Spiro-OMeTAD devices exhibit a higher average PCE above 11% (forward: 11.2%; reverse: 11.2%) while P3HT devices are only ~8% (forward: 7.2%; reverse: 8.6%). Figure S3 shows the improvements for PV parameters, *J*<sub>SC</sub> exhibits a consistent enhancement under both indoor and 1-sun lighting conditions for Spiro-OMeTAD (forward scan: 19.0 mA cm<sup>-2</sup> vs. 15.3 mA cm<sup>-2</sup>; reverse scan: 17.9 mA cm<sup>-2</sup> vs. 13.8 mA cm<sup>-2</sup>), *V*<sub>OC</sub> also shows an improvement from 0.87 V of P3HT devices to 0.96 V for Spiro-OMeTAD devices for their forward scan performance, which further indicates the superior performance for Spiro-OMeTAD devices.

Since *J*-*V* hysteresis exists for both Spiro-OMeTAD and P3HT HTL devices, MPPT measurement was carried out on devices to evaluate the valid steady-state PCE. From figure 1(e), Spiro-OMeTAD devices show a MPPT PCE of 17.9%, which is higher than P3HT devices (11.4%) under indoor lighting conditions. This PCE for Spiro-OMeTAD corresponds to a good power output density of 53.7 μW cm<sup>-2</sup>. In addition, figure 1(f) shows the MPPT PCE under 1 sun condition: a much higher MPPT PCE of 13.0% was measured for Spiro-OMeTAD device compared to P3HT (6.2%).



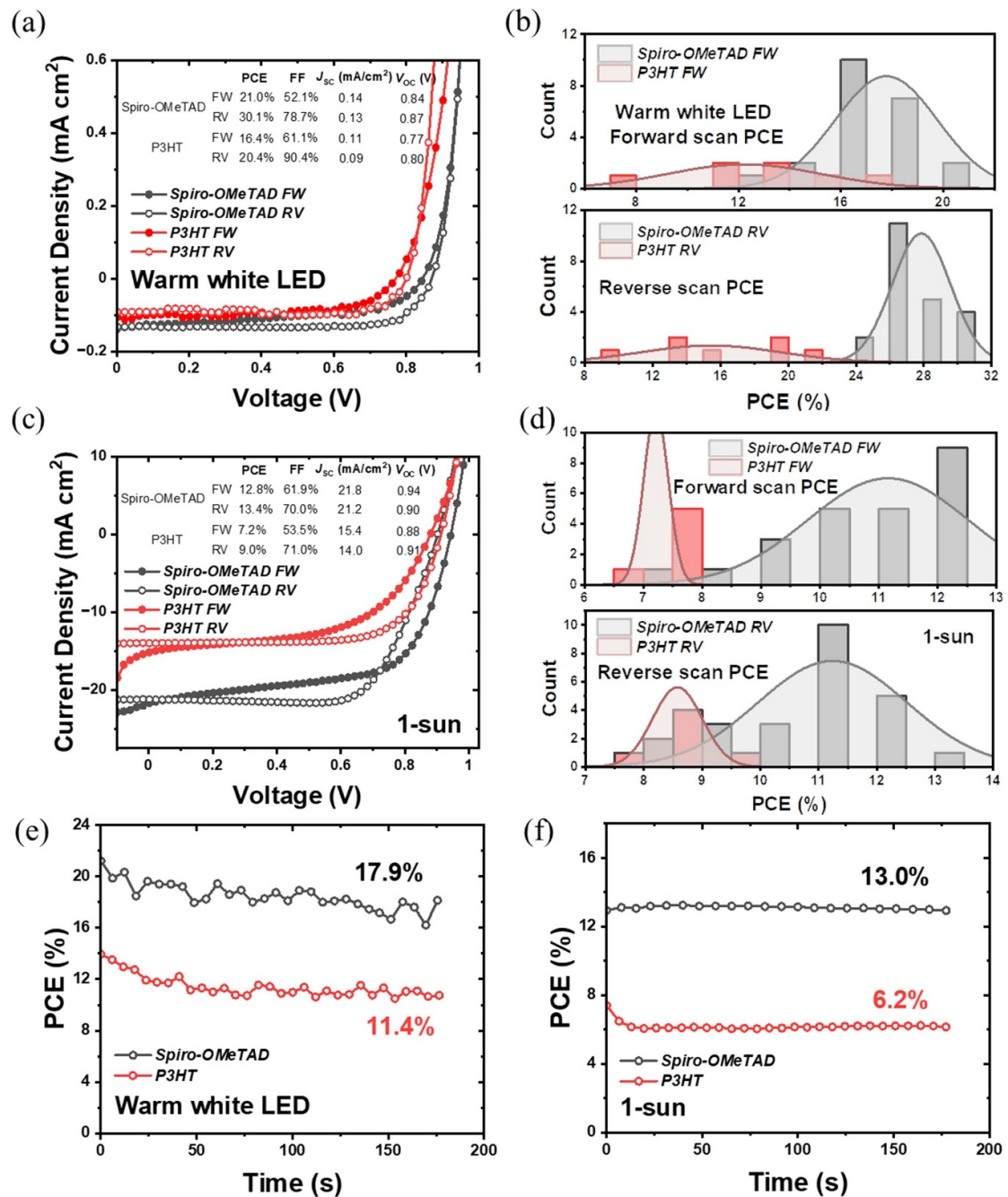


**Figure 1.** (a) Champion  $J$ - $V$  curves of Spiro-OMeTAD and P3HT HTL-based devices under warm white LED illumination. (b) The statistical distribution of PCE values of Spiro-OMeTAD and P3HT devices under 1000 lux warm white LED light. (c) Champion  $J$ - $V$  curves of Spiro-OMeTAD and P3HT based devices under 1 sun illumination. (d) The statistical distribution of PCE values of Spiro-OMeTAD and P3HT devices under 1 sun. (e) Maximum power point tracking PCE comparison of Spiro-OMeTAD and P3HT devices under warm white LED illumination. (f) Maximum power point tracking PCE comparison of Spiro-OMeTAD and P3HT devices under 1 sun condition.

A comparison of the EQE spectra of both devices is given in figure 2(a). The significantly higher EQE for Spiro-OMeTAD devices further proves the superiority of Spiro-OMeTAD as the HTL for indoor PV devices compared to P3HT. The integrated  $J_{SC}$  for Spiro-OMeTAD and P3HT devices are  $0.11 \text{ mA cm}^{-2}$  and  $0.07 \text{ mA cm}^{-2}$  under indoor light. From statistics of  $J_{SC}$  obtained from figure S3(b), the average  $J_{SC}$  measured from current-voltage measurements is  $\sim 0.14 \text{ mA cm}^{-2}$  and  $\sim 0.09 \text{ mA cm}^{-2}$  for Spiro-OMeTAD and P3HT devices, respectively. The  $J_{SC}$  estimated from EQE measurements is slightly lower compared to that from current-voltage measurements. This slight discrepancy has been previously noticed in perovskite PVs and could be due to various reasons as reported by Saliba and Etgar [38]. For example, the duration of EQE measurement is relatively slow since it needs to record the photocurrent for each wavelength while  $J$ - $V$  measurement is transient, so EQE measurement will be affected by ion migration in active layers, resulting in

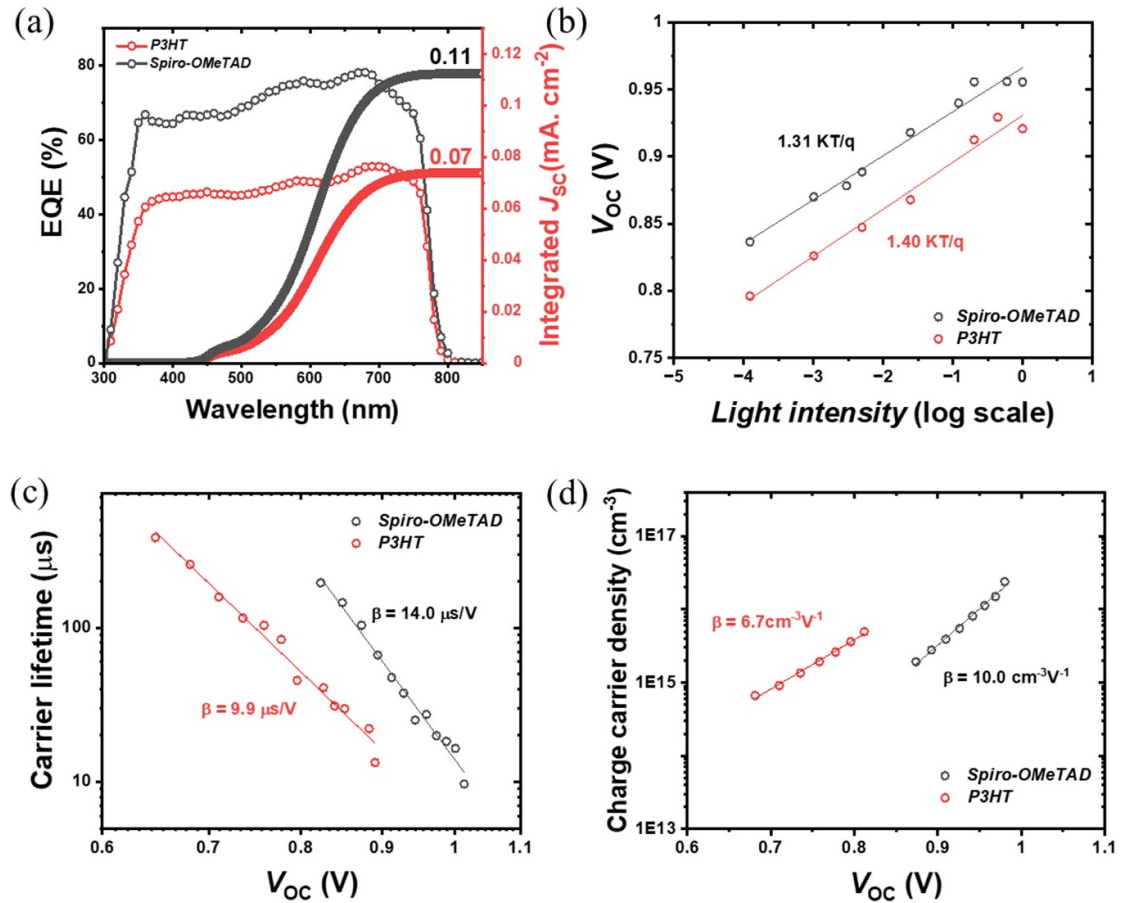


**Figure 2.** (a) EQE spectra of Spiro-OMeTAD device and P3HT HTL-based devices and the integrated  $J_{sc}$  under warm white LED ( $0.32 \text{ mW cm}^{-2}$ ). (b) Light intensity-dependent  $V_{oc}$  variation versus light intensity. (c) Transient photovoltage (TPV) characterization of Spiro-OMeTAD and P3HT HTL-based devices. (d) Transient photocurrent (TPC) characterization of Spiro-OMeTAD and P3HT HTL-based devices.

a lower photocurrent. As shown in figures 1(a) and (c) both devices show slight  $J$ - $V$  hysteresis and previously authors have shown that n-i-p MAPI devices with  $\text{SnO}_2$  and  $\text{TiO}_2$  as ETL shows enhanced hysteresis compared to the p-i-n MAPI devices under indoor lighting conditions [39]. Furthermore, an additional voltage bias is applied in  $J$ - $V$  measurement while EQE has none, and the applied bias will result in additional built-in potential at the interfaces, thus leading to higher current.

Noticeably, the deviation of PCE between Spiro-OMeTAD and P3HT devices becomes larger while changing the illumination source from 1 sun to indoor lighting (figures 1(a) and (c)). To investigate the reason for the lower performance of P3HT-based devices, light intensity-dependent  $J$ - $V$  characterizations were carried out, as this measurement can reveal the presence of trap-assisted recombination losses. Figure 2(b) shows the  $V_{oc}$  as a function of light intensity and that Spiro-OMeTAD device shows an ideality factor of 1.31, which is lower than that of P3HT devices (1.40), indicating less trap-assisted recombination for Spiro-OMeTAD devices. To further investigate the reasons for improvements in PCE brought by Spiro-OMeTAD over P3HT-based HTL, carrier lifetime and charge extraction properties of the devices were measured using TPV and TPC measurements. Figure 2(c) shows the carrier lifetime variation as a function of  $V_{oc}$  (equivalent to a variation of carrier lifetime as a function of light intensity) and revealed that the carrier lifetime of Spiro-OMeTAD devices is consistently higher than P3HT HTL based devices. This enhanced carrier lifetime will improve the charge extraction/collection to the respective electrodes and can thus account for the improved PCE of Spiro-OMeTAD HTL-based devices. The relationship of carrier lifetime versus  $V_{oc}$  in TPV measurement is given below as equation (1) [40]:

$$\tau = \tau_0 e^{-\beta V_{oc}}, \quad (1)$$

where  $\tau$  is the carrier lifetime,  $\beta$  is the decay constant extracted by fitting TPV data. The decay constant  $\beta$  for Spiro-OMeTAD and P3HT devices are  $14.0 \mu\text{s V}^{-1}$  and  $9.9 \mu\text{s V}^{-1}$ . The enhanced carrier lifetime for Spiro-OMeTAD devices further suggests better interfacial conditions. Figure 2(d) shows the TPC charge extraction results and the fitting equation (2) used is shown below [40]:

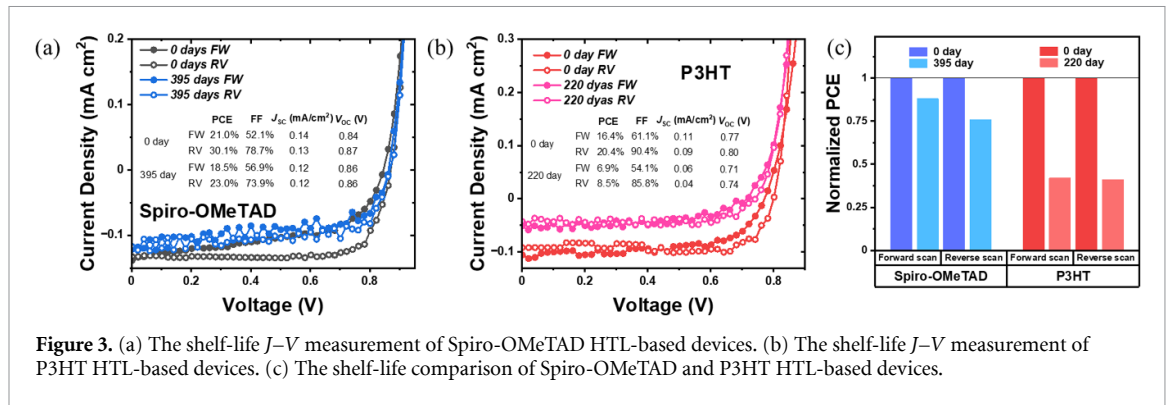


**Figure 3.** (a) The shelf-life  $J$ - $V$  measurement of Spiro-OMeTAD HTL-based devices. (b) The shelf-life  $J$ - $V$  measurement of P3HT HTL-based devices. (c) The shelf-life comparison of Spiro-OMeTAD and P3HT HTL-based devices.

$$n = n_0 e^{\gamma V_{oc}}, \quad (2)$$

where  $n$  is the carrier density. The  $\gamma$  parameter is the rate of charge carrier density versus light intensity and it has a value of  $19 \text{ V}^{-1}$  for ideal semiconductor [40]. From figure 2(d), the higher  $\gamma$  parameter ( $10.0 \text{ cm}^{-3} \text{ V}^{-1}$ ) for Spiro-OMeTAD devices indicates better charge transportation at perovskite/HTL interfaces. In contrast, the  $\gamma$  parameter for P3HT devices is  $6.7 \text{ cm}^{-3} \text{ V}^{-1}$ , the larger discrepancy of  $\gamma$  parameter indicates the significant level of non-radiative recombination losses for P3HT HTL based devices, which indicates the higher ratio of charge carriers will be captured by traps rather than transfer to the HTL, hence the short circuit current is reduced. The trapped charge carriers also limit the quasi-fermi level splitting and result in lower  $V_{oc}$  [41]. The enhanced carrier lifetime and interfacial conditions further suggest Spiro-OMeTAD is the better hole transport material for indoor halide perovskite PV devices compared to the P3HT.

Thus, a comparison of the PCE values from the  $J$ - $V$  characteristics and MPPT measurements reveals that P3HT HTL-based PVs show consistently lower performance metrics ( $V_{oc}$ ,  $J_{sc}$  and Fill Factor (FF)) compared to the Spiro-OMeTAD. Since Spiro-OMeTAD and P3HT have very similar HOMO levels, the observed differences in the PV performance parameters should stem from reasons other than the energy band alignment [42, 43]. Figure S4 shows the corresponding energy level diagram for the  $\text{CH}_3\text{NH}_3\text{PbI}_3$  n-i-p solar cells using Spiro-OMeTAD and P3HT as HTLs. In this case, the improved PV parameters ( $V_{oc}$  and  $J_{sc}$ ) for Spiro-OMeTAD HTL based devices can be attributed to the enhanced charge carrier lifetime (as revealed through the TPV measurements in figure 2(c)), lower trap-assisted recombination losses (as shown in the  $V_{oc}$  vs light intensity measurements in figure 2(b)) and the better charge extraction (as revealed through the TPC measurements in figure 2(d)) compared to that of P3HT HTL based devices. This better charge extraction in the Spiro-OMeTAD HTL-based devices is further evidenced through their improved fill factor as well ( $\sim 65\%$  vs  $\sim 55\%$ ) under 1 sun and ( $\sim 50\%$  vs  $20\%$ ) indoor light as shown in figure S3(a).

The poor charge extraction at the perovskite/P3HT interface can be attributed to the poor physical and electronic contact of the P3HT to the perovskite surface [31, 44]. The poor physical contact is due to the difference in surface energy between the P3HT and perovskite active layer which in turn reduces the contact surface area, detrimentally affecting the charge extraction. The poor electronic contact is due to the low degree of intrachain ordering of the P3HT on the perovskites or the 'edge on' stacking arrangement which promotes non-radiative loss at the P3HT/Perovskite interface [45].

Besides the enhanced optoelectronic properties, the stability of the indoor PV device is a critical part of practical application. A shelf-life stability comparison of the two types of devices is shown in figure 3. These devices were kept in the dark and dry air ambient conditions with a relative humidity of 11% and at a temperature of  $22^\circ\text{C}$ . They were kept under dry air conditions as previously it has been shown that in the presence of moisture (high relative humidity  $>50\%$ )  $\text{CH}_3\text{NH}_3\text{PbI}_3$  films and devices undergo decomposition due to hydration and subsequent deprotonation of the methyl ammonium cation. This decomposition is initiated by the hydrogen bonding interaction between the water molecules and the methyl ammonium cation leading to the formation of methyl amine and hydrogen iodide (HI) [46, 47].

Spiro-OMeTAD device shows an indoor PCE of 18.5% (forward scan) and 23.0% (reverse scan) after 395 days in figure 3(a). The Spiro-OMeTAD could maintain more than 85% of the initial performance over a year, while the performance of P3HT devices dropped to 6.9% (forward scan) and 8.5% (reverse scan) and could retain only  $\sim 40\%$  of the original PCE as shown in figure 3(b). Figure 3(c) shows a comparison of the shelf-life stability in the chart format. This poor shelf-life stability of P3HT based devices can be due to the formation of shunting paths/holes created in the HTL due to the degradation of the perovskite layer [45]. The poor physical contact with the perovskite active layer and the presence of traps can make the perovskite



layer in P3HT HTL-based devices more susceptible to moisture, oxygen and light, thus accelerating the device degradation [46]. Since the Spiro-OMeTAD based devices were showing better PV device performance and much better shelf-life stability compared to the P3HT-based devices, the former devices were then used for self-powering of the motion sensors as discussed in the next section.

### 3.2. Self-powering of motion sensors using Spiro-OMeTAD HTL-based indoor PV devices

Although various types of motion sensors have been developed, their practical applications in a system level for wearable electronics are still challenging [48, 49]. Generally, the external power source which can hinder volume miniaturization and weight reduction is required for operating the sensors directly attached to the human body [50]. The numerous amount of these devices, which are potentially going to reach one trillion nodes, raise a challenge to build a sustainable and reliable powering system to support them to operate [2]. The powering for smart sensor systems integrated with IoTs should provide sufficient power to operate various electronic components which collect, process, and transmit data obtained from the sensor, in addition to the sensing operation [51, 52]. Typically, the conventional battery-based powering has been used to enable the operation of the whole electronic components in the smart sensor system. However, the battery-based powering system has various drawbacks including limited lifetime, additional maintenance and interrupted operation and potential environmental harm [53]. Hence, big efforts to develop self-powering systems based on indoor PV cells which harvest light energy inside the buildings have been intensively investigated to overcome such issues induced by the battery-based powering system [53]. To meet the energy demand required for the self-powering of the whole smart sensor unit, the integration of indoor PVs with the energy storage components such as supercapacitors and rechargeable batteries might be necessary [2].

From this point of view, the Spiro-OMeTAD-HTL based indoor PV-powered sensor system including independent energy management and signal processing modules can be promising for wearable electronics operating under indoor light irradiation, which exhibits lightness, miniaturization, and continuous operation without an external power source. To demonstrate the feasibility of wearable self-powering motion sensors for real application, a strain sensor based on printed SWCNT random networks on the bendable/stretchable substrate of PDMS was integrated into the Spiro-OMeTAD-based sensor systems. The SWCNT-based strain sensor enabling to detect the human motion in real-time was selected as an active sensing device owing to its remarkable advantages including simple device configuration, low-voltage operation, high flexibility and mechanical robustness, and excellent sensitivity [54]. Figure 4(a) shows an optical image of the SWCNT random networks on the PDMS substrate fabricated by all solution-process at low temperature in ambient air, which exhibited excellent bendable and flexible properties. To characterize the electrical characteristics of the SWCNT-based strain sensor, the normalized resistance as a function of the bending strain was extracted from 4-point probe measurements. As shown in figure 4(b), the average of normalized resistance in SWCNT-based strain was linearly increased from 0 to  $124.1 \Omega \Omega^{-1}$  as the bending strain increased from 0% to 30%. Notably, the normalized resistance of ten samples fabricated in different batches at different times was characterized to demonstrate the reproducibility of SWCNT-based strain sensors, which indicates that good device-to-device uniformity was achieved with a relatively small difference in normalized resistance (under  $\sim 5\%$ ) over the whole bending strain range. Next, the sensitivity and linearity of the SWCNT-based strain sensor were determined using the following equation (3) [54]:

$$S = \delta \left( \frac{\Delta R}{R_0} \right) / \delta b \quad (3)$$

where  $S$  is sensitivity,  $R_0$  is the initial normalized resistance,  $\Delta R$  is the variation of the normalized resistance when bending strain is applied, and  $b$  is the bending strain. The proposed strain sensors exhibited high sensitivity of  $4.12\%^{-1}$  with good linearity ( $R^2 = 0.96881$ ). Figure S5 shows the hysteresis characteristics of SWCNT random networks as the strain sensor when the strain was applied and released. A very small hysteresis window was observed, indicating that the sensing operation of the proposed strain sensor was reliable for the detection of the applied strain in real time during the strain and release cycle. These advantages including high sensitivity, good linearity, and suppressed hysteresis are attributed to the random networks of SWCNTs distributed completely throughout the PDMS surface, as shown in the Atomic Force Microscopy (AFM) image of the inset of figure 4(b) [55–57]. Figure 4(c) shows the sensing mechanism of the flexible SWCNT random networks toward bending strain. As the applied strain is increased, the overall length of the conducting path between electrodes is increased, which increases the tunnelling distance between the SWCNTs and decreases the resistance of SWCNT random networks [56, 58]. On the other hand, the resistance returned to its initial state owing to the reduced tunnelling distance between the SWCNTs, as the applied strain is decreased and the conduction path between the electrode is reduced. Figures 4(d) and (e) show an optical image of the integrated sensor system based on the Spiro-OMeTAD-based power source

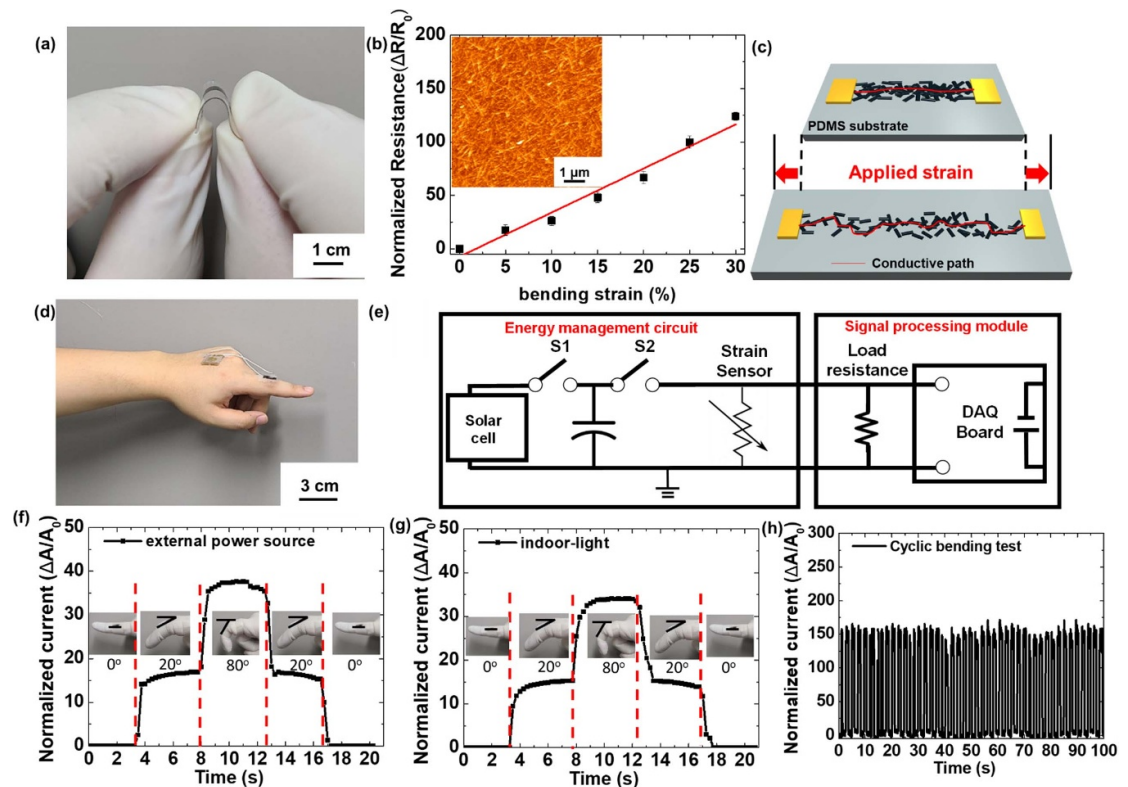


**Figure 4.** (a) Optical image of the flexible/bendable SWCNT random networks on the PDMS substrate proposed in this study. (b) Normalized resistance as a function of the bending strain extracted from four-point probe measurements (inset: morphological characteristics of the SWCNT random networks obtained from AFM measurements). (c) Illustration of the sensing mechanism of the flexible SWCNT random networks toward bending strain. (d) Optical image of the integrated sensor system based on the Spiro-OMeTAD-based power source and flexible SWCNT-based strain sensor directly attached to the human body. (e) Schematic circuit diagram of the self-powering motion sensor system consisting of energy management circuit and signal processing module. The normalized current was recorded by the data acquisition board at a sampling rate of 50 Hz upon the detection of movement on the human body using the SWCNT-based motion sensor with two differently charged sources: (f) the external power source and (g) the integrated Spiro-OMeTAD-based power source under indoor light irradiation. (h) The real-time response obtained from the Spiro-OMeTAD-based sensor system during cyclic bending tests including a position-controlled pressing/relaxing test with a bending strain of 30%.

and flexible SWCNT-based strain sensor directly attached to the human body and an illustration of the self-powering motion sensor system consisting of an energy management circuit and signal processing module. Under indoor light irradiation, the photo-generated electrons are charged in the supercapacitor (S1 is on and S2 is off). When no strain is applied, the supercapacitor starts discharging (S1 is off and S2 is on) by releasing the electrons through the strain sensor [59]. However, as the strain is increased upon human motion, which increases the resistance of the strain sensors accordingly, the electrons are released toward parallelly connected load resistance. As a result, the movement of the human body can be detected by analysing the change in the current of the load resistance in real-time, which was recorded by the data acquisition (DAQ) board (USB-101, JYTEK) at a sampling rate of 50 Hz. A separate power supply in the signal processing module was connected to the DAQ board to obtain a large amount of electric signals in real-time. Figures 4(f) and (g) show the simultaneous and continuous detection of movement on human body using the SWCNT-based motion sensor with two differently charged source: the external power source and the integrated Spiro-OMeTAD-based power source under indoor light irradiation, respectively. The SWCNT-based motion sensor with the external power source exhibited the normalized current of  $\sim 0$ ,  $\sim 16$ , and  $\sim 36$ , according to the finger angles of  $0^\circ$ ,  $20^\circ$ , and  $80^\circ$ , respectively. Very likely, similar electrical characteristics were recorded through the Spiro-OMeTAD-based motion sensor system exhibiting the normalized current of  $\sim 0$ ,  $\sim 15$  and  $\sim 34$ , according to the finger angles  $0^\circ$ ,  $20^\circ$ , and  $80^\circ$ , respectively. These results indicate that the comparable sensing performance can be obtained from the self-powering SWCNT-based motion sensor integrated with Spiro-OMeTAD-based power source under indoor light irradiation. To evaluate the operational stability of the proposed self-powering motion sensor system, time-domain cyclic tests were performed by monitoring the relative change in the normalized current as a function of bending strain in real-time. Figure S6 shows an optical image of custom-made strain measurement system consisting of a computer-controlled stepping motor and a source meter utilized in this

study to perform the cyclic bending tests including a position-controlled pressing/relaxing test with bending strain of 30%. Figures 4(h) and S7 show that the proposed self-powering motion sensor exhibited good repeatability without any conspicuous degradation of mechanical stability during the bending and releasing cycles, which indicate that Spiro-OMeTAD-HTL based energy harvesting can be promising for wearable self-powering electronics operating under indoor light irradiation.

## 4. Conclusion

A direct comparison of the hole extraction properties of two commonly used HTLs of Spiro-OMeTAD and P3HT was carried out in  $\text{CH}_3\text{NH}_3\text{PbI}_3$ -based PV devices under indoor illumination conditions. The Spiro-OMeTAD HTL-based devices outperform P3HT HTL-based devices both under 1 sun and indoor illumination conditions. Detailed optoelectronic characterization revealed that the origin of this enhanced performance for Spiro-OMeTAD HTL is related to better charge extraction and long carrier lifetime and reduced non-radiative losses. In addition to the enhanced performance, the Spiro-OMeTAD HTL-based devices show much better (85% vs 40%) retention of shelf-life stability as well compared to P3HT HTL-based devices. The best performing Spiro-OMeTAD HTL-based devices are then used to self-power a wearable motion sensor, which has an accurate and sensitive response to finger movement. Under indoor light illumination, the strain sensor successfully detects finger bending with different angles sharply. The successful sensor powering employing the indoor PV device indicates the good quality of the Spiro-OMeTAD HTL devices and the feasibility of the indoor PV device-sensor integration in the future IoT ecosystem.

## Data availability statement

The data that support the findings of this study are openly available at the following URL/DOI: <https://doi.org/10.17630/d943738d-b76f-4e64-9369-b2ffcae5a88b>.

## Acknowledgments

L K J acknowledges funding from UKRI-Future Leaders Fellowship, University of St Andrews, UK NRF Korea government (MSIT) Kwangwoon University through MR/T022094/1. This work was supported by the National Research Foundation of Korea (NRF) Grant funded by the Korea government (MSIT) (NRF-2021R1A2C2012855) and Kwangwoon university in 2023.

## Conflict of interest

The authors declare no conflict of interest.

## ORCID iDs

Tae-Jun Ha  <https://orcid.org/0000-0002-0935-795X>

Lethy Krishnan Jagadamma  <https://orcid.org/0000-0002-4339-2484>

## References

- [1] Wang K L, Zhou Y H, Lou Y H and Wang Z K 2021 Perovskite indoor photovoltaics: opportunity and challenges *Chem. Sci.* **12** 11936–54
- [2] Pecunia V, Occhipinti L G and Hoye R L Z 2021 Emerging indoor photovoltaic technologies for sustainable internet of things *Adv. Energy Mater.* **11** 2100698
- [3] Kim J et al 2020 Chlorine incorporation in perovskite solar cells for indoor light applications *Cell Rep. Phys. Sci.* **1** 100273
- [4] Mathews I, Kantareddy S N, Buonassisi T and Peters I M 2019 Technology and market perspective for indoor photovoltaic cells *Joule* **3** 1415–26
- [5] Kim G, Lim J W, Kim J, Yun S J and Park M A 2020 Transparent thin-film silicon solar cells for indoor light harvesting with conversion efficiencies of 36% without photodegradation *ACS Appl. Mater. Interfaces* **12** 27122–30
- [6] Wang Z, Tang A, Wang H, Guo Q, Guo Q, Sun X, Xiao Z, Ding L and Zhou E 2023 Organic photovoltaic cells offer ultrahigh VOC of ~1.2 V under AM 1.5G light and a high efficiency of 21.2% under indoor light *Chem. Eng. J.* **451** 139080
- [7] Zhang D and Medvedev P 2021 A molecular photosensitizer achieves a  $V_{oc}$  of 1.24 V enabling highly efficient and stable dye-sensitized solar cells with copper(II/I)-based electrolyte *Nat. Commun.* **12** 2–11
- [8] Teran A S, Wong J, Lim W, Kim G, Lee Y, Blaauw D and Phillips J D 2015 AlGaAs photovoltaics for indoor energy harvesting in mm-scale wireless sensor nodes *IEEE Trans. Electron Devices* **62** 2170–5
- [9] He X et al 2021 40.1% record low-light solar-cell efficiency by holistic trap-passivation using micrometer-thick perovskite film *Adv. Mater.* **33** 2100770
- [10] Guo Z, Jena A K and Miyasaka T 2022 Halide perovskites for indoor photovoltaics: the next possibility *ACS Energy Lett.* **8** 90–95
- [11] Muhammad B T, Kar S, Stephen M and Leong W L 2022 Halide perovskite-based indoor photovoltaics: recent development and challenges *Mater. Today Energy* **23** 100907

- [12] De Rossi F, Pontecorvo T and Brown T M 2015 Characterization of photovoltaic devices for indoor light harvesting and customization of flexible dye solar cells to deliver superior efficiency under artificial lighting *Appl. Energy* **156** 413–22
- [13] Li M, Igbari F, Wang Z K and Liao L S 2020 Indoor thin-film photovoltaics: progress and challenges *Adv. Energy Mater.* **10** 2000641
- [14] Lee C, Lee J H, Lee H H, Nam M and Ko D H 2022 Over 30% efficient indoor organic photovoltaics enabled by morphological modification using two compatible non-fullerene acceptors *Adv. Energy Mater.* **12** 1–10
- [15] Kim J *et al* 2022 Revisiting the classical wide-bandgap HOMO and random copolymers for indoor artificial light photovoltaics *Macromol. Rapid Commun.* **43** 1–11
- [16] Saeed M A, Kim T H, Ahn H, Park N W, Park J, Choi H, Shahzad A and Shim J W 2023 2D MXene additive-induced treatment enabling high-efficiency indoor organic photovoltaics *Adv. Opt. Mater.* **11** 1–11
- [17] Hyuk Kim T, Jin Chung J, Ahsan Saeed M, Youn Lee S and Won Shim J 2023 High-efficiency (over 33 %) indoor organic photovoltaics with band-aligned and defect-suppressed interlayers *Appl. Surf. Sci.* **610** 155558
- [18] Chen C, Nguyen V S, Chiu H-C, Chen Y-D, Wei T-C and Yeh C-Y 2022 Anthracene-bridged sensitizers for dye-sensitized solar cells with 37% efficiency under dim light (Adv. Energy Mater. 20/2022) *Adv. Energy Mater.* **12** 2270080
- [19] Mozaffari S, Nateghi M R and Zarandi M B 2017 An overview of the challenges in the commercialization of dye sensitized solar cells *Renew. Sustain. Energy Rev.* **71** 675–86
- [20] Shin S C, Koh C W, Vincent P, Goo J S, Bae J-H, Lee J-J, Shin C, Kim H, Woo H Y and Shim J W 2019 Ultra-thick semi-crystalline photoactive donor polymer for efficient indoor organic photovoltaics *Nano Energy* **58** 466–75
- [21] Habibi M, Zabihi F, Ahmadian-Yazdi M R and Eslamian M 2016 Progress in emerging solution-processed thin film solar cells—part II: perovskite solar cells *Renew. Sustain. Energy Rev.* **62** 1012–31
- [22] Schaller R D and Klimov V I 2004 High efficiency carrier multiplication in PbSe nanocrystals: implications for solar energy conversion *Phys. Rev. Lett.* **92** 1584–9
- [23] Dagar J, Castro-Hermosa S, Lucarelli G, Cacialli F and Brown T M 2018 Highly efficient perovskite solar cells for light harvesting under indoor illumination via solution processed SnO<sub>2</sub>/MgO composite electron transport layers *Nano Energy* **49** 290–9
- [24] Guo Z, Jena A K, Takei I, Ikegami M, Ishii A, Numata Y, Shibayama N and Miyasaka T 2021 Dopant-free polymer HTM-based CsPbI<sub>2</sub>Br solar cells with efficiency over 17% in sunlight and 34% in indoor light *Adv. Funct. Mater.* **31** 2103614
- [25] Bulloch A, Wang S, Ghosh P and Jagadamma L K 2022 Hysteresis in hybrid perovskite indoor photovoltaics *Phil. Trans. R. Soc. A* **380** 20210144
- [26] Jena A K, Kulkarni A and Miyasaka T 2019 Halide perovskite photovoltaics: background, status, and future prospects *Chem. Rev.* **119** 3036–103
- [27] Fu Q *et al* 2022 Ionic dopant-free polymer alloy hole transport materials for high-performance perovskite solar cells *J. Am. Chem. Soc.* **144** 9500–9
- [28] Chen Q, Wu J, Wang X, Li G, Song Z, Xu Y, Deng C, Weihai Sun Y D and Lan Z 2022 3-chloroperoxybenzoic acid doping spiroOMeTAD for improving the performance of perovskite solar cells *Chem. Eng. J.* **450** 138313
- [29] Bai S *et al* 2022 Ion-modulated radical doping of spiro-OMeTAD for more efficient and stable perovskite solar cells *Science* **501** 495–501
- [30] Yin X, Song Z, Li Z and Tang W 2020 Toward ideal hole transport materials: a review on recent progress in dopant-free hole transport materials for fabricating efficient and stable perovskite solar cells *Energy Environ. Sci.* **13** 4057–86
- [31] Jung E H, Jeon N J, Park E Y, Moon C S, Shin T J, Yang T-Y, Noh J H and Seo J 2019 Efficient, stable and scalable perovskite solar cells using poly(3-hexylthiophene) *Nature* **567** 511–5
- [32] Lee H K H *et al* 2019 Outstanding indoor performance of perovskite photovoltaic cells—effect of device architectures and interlayers *Sol. RRL* **3** 1–7
- [33] Sun J, Pu X, Liu M, Yu A, Du C, Zhai J, Hu W and Wang Z L 2018 Self-healable, stretchable, transparent triboelectric nanogenerators as soft power sources *ACS Nano* **12** 6147–55
- [34] Goo J S, Shin S C, You Y J and Shim J W 2018 Polymer surface modification to optimize inverted organic photovoltaic devices under indoor light conditions *Sol. Energy Mater. Sol. Cells* **184** 31–37
- [35] Koster L J A, Mihailetschi V D, Ramaker R and Blom P W M 2005 Light intensity dependence of open-circuit voltage of polymer:fullerene solar cells *Appl. Phys. Lett.* **86** 1–3
- [36] Green M A 1981 Solar cell fill factors: general graph and empirical expressions *Solid. State. Electron.* **24** 788–9
- [37] Jagadamma L K and Wang S 2021 Wide-bandgap halide perovskites for indoor photovoltaics *Front. Chem.* **9** 1–8
- [38] Saliba M and Etgar L 2020 Current density mismatch in perovskite solar cells *ACS Energy Lett.* **5** 2886–8
- [39] Elumalai N K and Uddin A 2016 Hysteresis in organic-inorganic hybrid perovskite solar cells *Sol. Energy Mater. Sol. Cells* **157** 476–509
- [40] Singh S and Kabra D 2021 Comparative study of recombination dynamics in optimized composition of Sn- versus Pb-based perovskite solar cells *ACS Appl. Mater. Interfaces* **13** 42297–306
- [41] Lanz O 2018 Osteoplastische resection beider oberkiefer nach kocher—Eine neue Operationsmethode zur Freilegung der Schädelbasis und des Pharyngonasalraumes *Dtsch. Z. Chir.* **35** 423–32
- [42] Li S, Cao Y L, Li W H and Bo Z S 2021 A brief review of hole transporting materials commonly used in perovskite solar cells *Rare Met.* **40** 2712–29
- [43] Jiménez-López J, Cambarau W, Cabau L and Palomares E 2017 Charge injection, carriers recombination and HOMO energy level relationship in perovskite solar cells *Sci. Rep.* **7** 1–10
- [44] Gu W M, Jiang K-J, Li F, Yu G-H, Xu Y, Fan X-H, Gao C-Y, Yang L-M and Song Y 2022 A multifunctional interlayer for highly stable and efficient perovskite solar cells based on pristine poly(3-hexylthiophene) *Chem. Eng. J.* **444** 136644
- [45] Xu D, Gong Z, Jiang Y, Feng Y, Wang Z, Gao X, Lu X, Zhou G, Liu J-M and Gao J 2022 Constructing molecular bridge for high-efficiency and stable perovskite solar cells based on P3HT *Nat. Commun.* **13** 1–8
- [46] Yang J and Kelly T L 2017 Decomposition and cell failure mechanisms in lead halide perovskite solar cells *Inorg. Chem.* **56** 92–101
- [47] Townsend N and Amit I 2019 The future is flexible *Phys. World* **32** 35–38
- [48] Wang J, Lu C and Zhang K 2020 Textile-based strain sensor for human motion detection *Energy Environ. Mater.* **3** 80–100
- [49] Kim M 2021 Assessment of the effect on the human body of the flicker of OLED displays of smartphones *J. Inf. Disp.* **22** 269–74
- [50] Attal F, Mohammed S, Dedabrishvili M, Chamroukhi F, Oukhellou L and Amirat Y 2015 Physical human activity recognition using wearable sensors *Sensors* **15** 31314–38
- [51] Khan Y, Thielens A, Muin S, Ting J, Baumbauer C and Arias A C 2020 A new frontier of printed electronics: flexible hybrid electronics *Adv. Mater.* **32** 1–29
- [52] Portilla L *et al* 2022 Wirelessly powered large-area electronics for the internet of things *Nat. Electron.* **6** 10–7

- [53] Shen D, Duley W W, Peng P, Xiao M, Feng J, Liu L, Zou G and Zhou Y N 2020 Moisture-enabled electricity generation: from physics and materials to self-powered applications *Adv. Mater.* **32** 1–31
- [54] Kim S J, Song W, Yi Y, Min B K, Mondal S, An K-S and Choi C-G 2018 High durability and waterproofing rGO/SWCNT-fabric-based multifunctional sensors for human-motion detection *ACS Appl. Mater. Interfaces* **10** 3921–8
- [55] Ahuja P, Akiyama S, Ujjain S K, Kukobat R, Vallejos-Burgos F, Futamura R, Hayashi T, Kimura M, Tomanek D and Kaneko K 2019 A water-resilient carbon nanotube based strain sensor for monitoring structural integrity *J. Mater. Chem. A* **7** 19996–20005
- [56] Jeon J Y and Ha T J 2016 Waterproof electronic-bandage with tunable sensitivity for wearable strain sensors *ACS Appl. Mater. Interfaces* **8** 2866–71
- [57] Schnittker K, Tursunniyaz M and Andrews J B 2021 Recent advances in printable carbon nanotube transistors for large-area active matrices *J. Inf. Disp.* **22** 193–209
- [58] Kang B C, Park S J and Ha T J 2021 Wearable pressure/touch sensors based on hybrid dielectric composites of zinc oxide nanowires/poly(dimethylsiloxane) and flexible electrodes of immobilized carbon nanotube random networks *ACS Appl. Mater. Interfaces* **13** 42014–23
- [59] Li P, Wen Y, Liu P, Li X and Jia C 2010 A magnetoelectric energy harvester and management circuit for wireless sensor network *Sens. Actuators A* **157** 100–6